ACS APPLIED MATERIALS & INTERFACES

www.acsami.org

Research Article

# $CuInS_2$ Photocathodes with Atomic Gradation-Controlled $(Ta,Mo)_x(O,S)_y$ Passivation Layers for Efficient Photoelectrochemical $H_2$ Production

Sang Youn Chae,[#] Yoolim Kim,[#] Eun Duck Park, Sang Hyuk Im, and Oh-Shim Joo*

Cite This: https://doi.org/10.1021/acsami.1c09560

Read Online

ACCESS | Metrics & More | Article Recommendations | Supporting Information

**ABSTRACT:** An atomic gradient passivation layer, $(Ta,Mo)_x(O,S)_y$, is designed to improve the charge transportation and photoelectrochemical activity of $CuInS_2$-based photoelectrodes. We found that Mo spontaneously diffused to the a-$TaO_x$ layer during e-beam evaporation. This result indicates that the gradient profile of $MoO_x/TaO_x$ is formed in the sublayer of $(Ta,Mo)_x(O,S)_y$. To understand the atomic-gradation effects of the $(Ta,Mo)_x(O,S)_y$ passive layer, the composition and (photo)electrochemical properties have been characterized in detail. When this atomic gradient-passive layer is applied to $CuInS_2$-based photocathodes, promising photocurrent and onset potential are seen without using Pt cocatalysts. This is one of the highest activities among reported $CuInS_2$ photocathodes, which are not combined with noble metal cocatalysts. Excellent photoelectrochemical activity of the photoelectrode can be mainly achieved by (1) the electron transient time improved due to the conductive Mo-incorporated $TaO_x$ layer and (2) the boosted electrocatalytic activity by $Mo_x(O,S)_y$ formation.

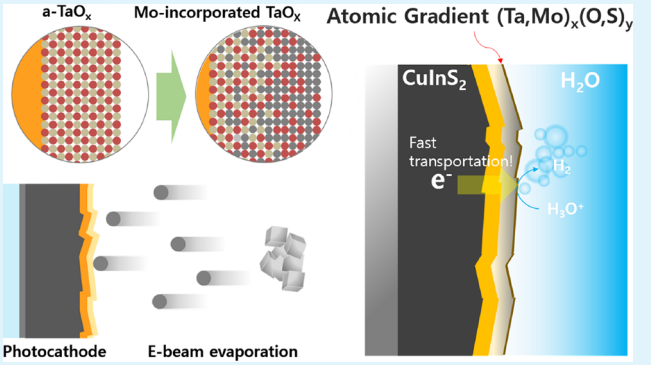


**KEYWORDS:** *tantalum oxide, passivation layer, photoelectrochemical cell, $CuInS_2$, atomic gradation*

## 1. INTRODUCTION

p-$CuInS_2$ is one of the promising materials as photoelectrodes for solar energy harvesting and photoelectrochemical hydrogen production. It has a ~1.5 eV band gap, which can absorb light of a wide wavelength range from the solar spectrum, and has a higher conduction band position than the redox potential of hydrogen evolution in aqueous media.[1,2] Moreover, the direct band gap property of $CuInS_2$ allows for intensive light absorption on the order of $\sim 10^5$ of the absorption coefficient.[3,4] For efficient photoelectrochemical hydrogen evolution reaction (HER), investigating the interface between p-type semiconductor photocathodes and electrolytes is required. At photocathode/electrolyte interfaces, built-in potential is generated at the space charge region due to band-bending in the energy structure of semiconductors. Especially, suppressing defect sites is one of the key strategies in improving the photoelectrochemical reaction efficiency because these are related to electron−hole recombination at semiconductor electrodes.[5−7]

Generally, defect sites can be diminished by deposition of passive layers. Passive layers on semiconductor electrodes were originally used to reduce (photo)corrosion during a photoelectrochemical reaction. Metal oxides are widely used for protection and/or as a passive layer for $CuInS_2$ or even other p-type photocathode materials.[8−10] However, surface layers can also be used to control the surface properties of semiconductors and band alignment, which affect electron−hole recombination or charge transfer at the interface between semiconductors and electrolytes.[11−13] An ideal passivation layer has to have less light absorption, a suitable band gap position compared to semiconductor materials, high stability, and high catalytic activity for the desired reaction. However, it is hard to meet these requirements with only one single material. Therefore, some researchers have designed multilayer-structured or multicomponent passive layers.[14−18]

Some researchers have suggested passivation layers that have an atomically graded structure.[19,20] The Turner and Gu group reported the $MoS_x/MoO_x/TiO_2$ graded layer for a $GaInP_2$ photocathode.[19] In the study, catalytic $MoS_x$ was hybridized with a passive $TiO_2$ layer, and then the hybridized layer showed better catalytic activity and stability for the photoelectrochemical reaction due to the formation of a chemically protected and electronically conductive $MoO_x$ layer. The Wang group reported a $TiO_2$ protective layer graded with

Received: May 23, 2021
Accepted: August 18, 2021

**Scheme 1. Schematic Diagram of the Preparation Process for $CuInS_2$/CdS/$(Ta,Mo)_x(O,S)_y$ Photocathodes**

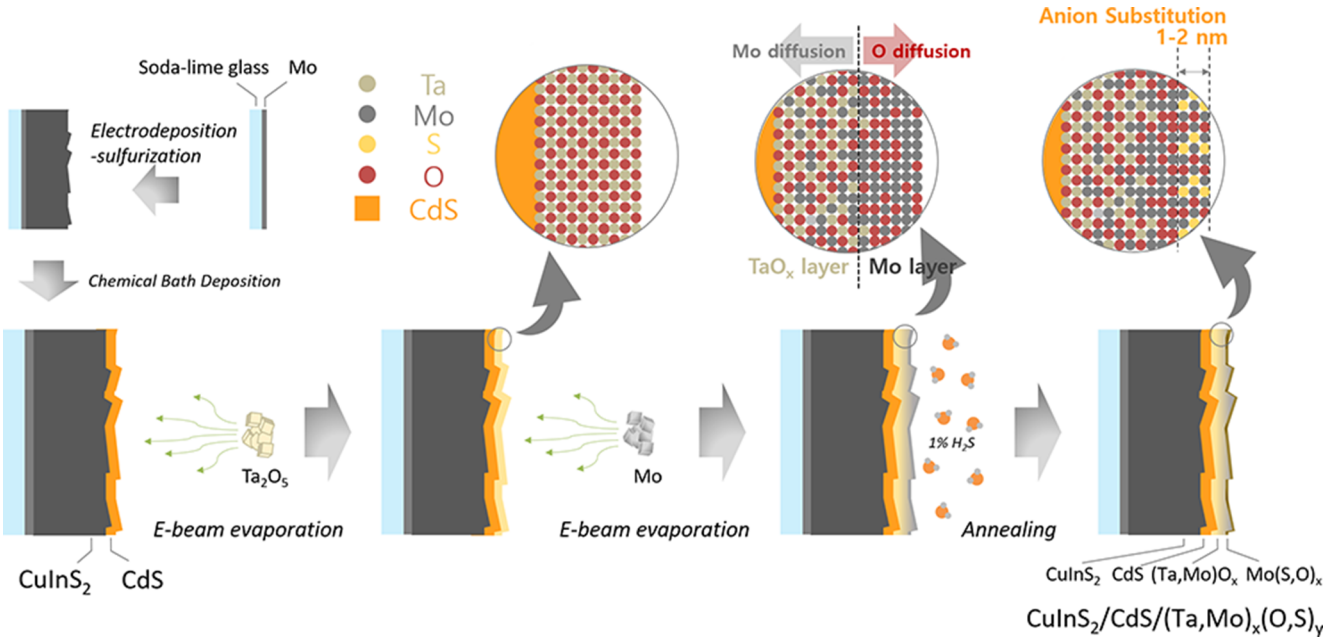


oxygen defects on Si-based photocathodes, where the gradient oxygen defect improved charge transport.[20] The graded atomic profile of heteroatoms in the passivation layer improved catalytic activity, carrier transportation efficiency, and photostability during the photoelectrochemical reaction.

Our group also reported a novel $TaO_x$ multifunctional passive layer for a $CuInS_2$ photocathode.[21] Tantalum oxide has good passivation ability with suppression of electron−hole pair recombination but has insufficient catalytic activity for hydrogen evolution. However, amorphous tantalum oxide was converted to the tantalum hydroxide/oxide hybrid structure by an in situ photoelectrochemical reaction. Hybridization of hydroxide/oxide shows multifunctional effects, which are passivation, protection, and catalytic activity. Therefore, passivation layer hybridization with catalysts can be an advantageous strategy to improve the activity of various semiconductor materials.

In this work, we have designed a gradient layer with a $(Ta,Mo)_x(O,S)_y$ alloy for $CuInS_2$ photocathodes based on our previous study on $TaO_x$ passivation layers. The $(Ta,Mo)_x(O,S)_y$ alloy has an atomic gradient profile with a Mo-/S-rich surface. $MoS_x$ is a well-known efficient catalyst for HER,[22−24] and $TaO_x$ is an effective protection and passivation layer for suppressing electron−hole recombination.[21] Therefore, we prepared a $TaO_x$ layer first and then deposited Mo with 2−30 nm thickness on the $TaO_x$ layer by e-beam evaporation. As a result of e-beam evaporation, Mo-incorporated $TaO_x$ layers (Mo−Ta−O) are obtained. Then, a gradient-$(Ta,Mo)_x(O,S)_y$ layer was obtained by annealing the Mo−Ta−O layer under a $H_2S$ atmosphere (Scheme 1).

We found that Mo atoms were transformed into a molybdenum oxysulfide form with a 1−2 nm thickness at the surface, which has high electrochemical HER activity. Also, a significantly reduced electron transient time is observed from the $TaO_x$ layer incorporated with Mo atoms. With the synergetic effects of the gradient $(Ta,Mo)_x(O,S)_y$ layer, the $CuInS_2$/CdS/$(Ta,Mo)_x(O,S)_y$ photocathode shows promising photoelectrochemical activity with an ∼11 mA·cm$^{-2}$ photocurrent density at 0 $V_{RHE}$ and onset potential of 0.55 $V_{RHE}$. This activity is comparable to that of a typical Pt-decorated $CuInS_2$ photocathode, and this result is the highest photoelectrochemical activity among reported $CuInS_2$ photocathodes without noble Pt cocatalysts. This suggested that heteroatom incorporation into a passive layer is a promising strategy for boosting the charge transport in semiconductor electrodes.

## 2. EXPERIMENTAL SECTION

**2.1. Preparation of $CuInS_2$ and CdS Layers.** $CuInS_2$ films were deposited by electrodeposition using asulfurization method. Cu and In layers were subsequently deposited by electrodeposition on a 500 nm Mo-coated soda-lime glass substrate. For Cu deposition, a potential of −0.5 $V_{Ag/AgCl}$ was applied to the Mo/soda-lime glass substrate for 1650 s in an electrolytic bath of 0.01 M $CuSO_4·5H_2O$ (Sigma-Aldrich, 99.95%) and 0.01 M citric acid (Sigma-Aldrich, 99.5%). For In deposition, a potential of −0.78 $V_{Ag/AgCl}$ was applied to the Cu-deposited substrate for 1780 s in an electrolytic bath of 0.03 M $InCl_3$ (Sigma-Aldrich, 99.999%), 0.036 M sodium citrate (Sigma-Aldrich, 99.5%), and 0.01 M citric acid (Sigma-Aldrich, 99.9%). Then, the Cu/In-deposited substrate was subsequently annealed in a $N_2$ atmosphere at 110 °C for 1 h and in a 1% $H_2S$ ($N_2$ balance) atmosphere at 520 °C for 1 h. The annealed $CuInS_2$ film was etched in 0.1 M KCN (Sigma-Aldrich, 98%) for 30 s. A CdS film was deposited on the $CuInS_2$ layer by chemical bath deposition. The substrate deposited with $CuInS_2$ was dipped in a chemical bath (a mixture of 20 mL of 0.015 M $CdSO_4$ (Sigma-Aldrich, 99%) and 26 mL of $NH_4OH$ (Junsei, 28%) aqueous solution). The bath was heated up to 70 °C, and then 10 mL of 0.1 M thiourea (Sigma-Aldrich, 99%) aqueous solution was added to the chemical bath solution. The substrate was removed from the chemical bath after 7 min, then washed with distilled water, and dried by a $N_2$ stream.

**2.2. Preparation of Passivation Layers.** A gradient $(Ta,Mo)O_x$ layer was prepared by the sequential deposition of $Ta_2O_5$ and Mo on a $CuInS_2$/CdS film using an e-beam evaporator (KVE-E2006, Korea Vacuum Tech). First, a 20 nm $TaO_x$ layer was deposited with $Ta_2O_5$ pellets (LTS Research Laboratories, Inc., 99.995%). Mo films of 2−30 nm thickness were deposited on the $TaO_x$ layer with Mo metal pellets (Taewon Scientific CO., Ltd, 99.95%) as an e-beam source. For transformation to $(Ta,Mo)_x(O,S)_y$, the $CuInS_2$/CdS film deposited with $(Ta,Mo)O_x$ was annealed at 200 °C in a 1% $H_2S$ ($N_2$ balance)


https://doi.org/10.1021/acsami.1c09560
ACS Appl. Mater. Interfaces XXXX, XXX, XXX−XXX

atmosphere. For a reference photocathode ($CuInS_2$/CdS/$TaO_x$/Pt), only $TaO_x$ was deposited on a $CuInS_2$/CdS film using an e-beam evaporator under the same condition. Then, $CuInS_2$/CdS/$TaO_x$ was decorated with Pt nanoparticles by electrodeposition with an applied potential condition of −0.1 $V_{Ag/AgCl}$ for 45 s in an electrolytic bath of 0.001 M $H_2PtCl_6{\cdot}6H_2O$ (Sigma-Aldrich, >37.5% Pt basis) aqueous solution.

**2.3. Photoelectrochemical Characterization.** All of the (photo)electrochemical characterizations were carried out using a potentiostat (Iviumstat, Ivium Technology) with a conventional three-electrode configuration with $CuInS_2$-based photocathodes as the working electrode, a platinum counter electrode, and a Ag/AgCl reference electrode. A 0.1 M $HClO_4$ aqueous solution (pH 1.07−1.08) was used as the electrolyte for all of the photoelectrochemical characterizations. The applied potential vs the Ag/AgCl reference electrode ($E_{Ag/AgCl}$) was converted to the $E_{RHE}$, potential vs a reversible hydrogen electrode (RHE), by eq 1, where $E_{Ag/AgCl}$ is the applied potential vs the Ag/AgCl reference electrode for the working electrode, pH is the pH value of the electrolyte, and $E^{\circ}_{Ag/AgCl}$ is the standard redox potential of the $AgCl + e^- \leftrightharpoons Ag + Cl^-$ reaction in the reference electrode (0.209 V)

$$E_{Ag/AgCl}(V) + (0.0591 \times pH) + E^{\circ}_{Ag/AgCl} = E_{RHE}(V) \quad (1)$$

Linear sweep voltammetry was used for investigating $I-V$ curves under light-chopping conditions with a 10 mV $s^{-1}$ scan rate. The light source was a solar simulator equipped with a 300 W Xe lamp and an air mass 1.5 filter. Light intensity was calibrated using a reference solar cell as 1 sun (100 mW $cm^{-2}$). The stability test of $CuInS_2$/CdS/$TaO_x$/Pt or $CuInS_2$/CdS/$(Ta,Mo)_x(O,S)_y$ photocathodes was carried out using chronoamperometry with a three-electrode system similar to that used for LSV measurements under the 1 sun illumination condition at 0 $V_{RHE}$ applied potential. The half-cell applied bias photon to current conversion efficiency (HC-ABPE) was calculated by eq 2, where $|J|$ is the photocurrent density, $V_{applied}$ is the applied potential ($V$ vs RHE), and $P$ is the light intensity, 100 mW·$cm^{-2}$

$$\frac{|J| \times V_{applied}}{P} \times 100\% = \text{HC-ABPE}\ (\%) \quad (2)$$

Electrochemical impedance spectroscopy (EIS) was carried out to investigate charge transfer properties and reveal the capacitance behavior of surface states. EIS was performed in the frequency range from 1 to 20 000 Hz at each applied potential (0.1 to −0.35 $V_{Ag/AgCl}$) with 1 sun (100 mW $cm^{-2}$) light intensity. Intensity-modulated photocurrent spectroscopy (IMPS) was conducted to investigate the electron transient time ($\tau_d$) of several photocathodes using a potentiostat and a LED driver set (Autolab PGSTAT128N, Metrohm). IMPS was performed under the applied potential of 0 $V_{RHE}$, light illumination of a LED blue light (470 nm) with 10, 30, or 100 mW $cm^{-2}$ intensity, and the frequency range from 1 to 20 000 Hz. The photon flux ($\Phi$) of each LED light intensity was calculated to plot the log $\tau_d$–log $\Phi^{-0.5}$ graph, as eq 3, where $P_{light}$ is the light intensity (mW $cm^{-2}$), $\lambda$ is the wavelength of light (470 nm), $h$ is Plank constant ($4.135 \times 10^{-15}$ eV s), $c$ is the speed of light (299 792 458 m $s^{-1}$), and $q$ is the conversion factor of an electronvolt to joule ($1.602 \times 10^{-19}$)

$$\frac{P_{light} \times \lambda}{hc} = \frac{P_{light} \times \lambda}{q \times 1239.8\ (\text{eV nm})} = \Phi(\text{cm}^{-2}\ \text{s}^{-1}) \quad (3)$$

**2.4. Other Characterizations.** The morphology and elemental composition analyses for photocathodes were carried out using transmission electron microscopy (TEM, Tecnai F20 G2, FE), scanning electron microscopy (SEM, JSM-7900F, JEOL), and energy-dispersive X-ray spectroscopy (EDS). The chemical state of passive layers with depth profiling was characterized using X-ray photoelectron spectroscopy (XPS, PHI 5000 VersaProbe, ULVAC PHI). The sputtering rate with $Ar^+$ ions with 2 kV energy was calibrated using a $SiO_2$ reference sample (0.5 nm·$s^{-1}$). The transmittance of passive layers was measured using a UV−vis−NIR spectrometer (Agilent, Cary-5000), which was equipped with an integrated sphere. $H_2$ and $O_2$ gas amounts photoelectrochemically generated by photocathodes and a counter anode were measured using a gas chromatograph (YL6500 GC, Youngin Chromass) with a molecular sieve 5A column and a plasma discharge ionization detector (PDD) during chronoamperometry measurement under the 1 sun illumination condition. The faradic efficiency ($\eta_F$) of evolved $H_2$ and $O_2$ was calculated using eqs 4 and 5, where $\phi$ is the volumetric concentration of the produced gas ($H_2$ or $O_2$), $Q$ is the flow rate of the He carrier gas that is injected into the gas chromatograph (100 mL $min^{-1}$), $n$ is the equivalent electron number (2 or 4 for $H_2$ or $O_2$), $F$ is the Faraday constant (96485.3329 C $mol^{-1}$), $p$ is the pressure of a photoelectrochemical cell reactor (1 atm), $R$ is the ideal gas constant (0.082057 L atm $K^{-1}$ $mol^{-1}$), $T$ is the reactor temperature (298 K) of the photoelectrochemical cell, $I_\phi$ is the current that is calculated from the evolved gas amount, and $I_{stat}$ is the chronoamperometrical steady-state photocurrent during the photoelectrochemical reaction

$$\phi \times Q \times \frac{nFp}{RT} = I_\phi \quad (4)$$

$$\frac{I_\phi}{I_{stat}} \times 100\% = \eta_F \quad (5)$$

## 3. RESULTS AND DISCUSSION

**3.1. Characterization of $(Ta,Mo)_x(O,S)_y$ Passive Layers on a $CuInS_2$/CdS Film.** The morphology, crystallography, and chemical structure of a $CuInS_2$-based thin-film photocathode, $CuInS_2$/CdS/$(Ta,Mo)_x(O,S)_y$, which was prepared in several steps, were characterized using SEM-EDS, GIXRD, and XPS. The schematic diagram of the preparation process for the photocathode is shown in Scheme 1. The thickness of the tantalum oxide layer was controlled to 20 nm, and the thickness after deposition of molybdenum was changed to 2, 6, 12, and 30 nm. As a result, a passive layer, $(Ta,Mo)_x(O,S)_y$, was uniformly deposited on the surface of a $CuInS_2$/CdS film, as shown in the SEM images of the photocathode (Figures 1 and S1). Each atom of the photocathode film (Cu, In, S, Cd, Ta, Mo, and O) was confirmed by EDS spectra. The atomic percent of molybdenum in the EDS spectra is proportionally increased by the molybdenum thickness deposited by e-beam evaporation, except for the 2 nm Mo thickness (Figure S1 and Table S1), which is due to the amount of the molybdenum atom, which is below the detection limit of EDS.

The crystallinity of photocathode films was investigated using GIXRD spectra (Figure S2). Regardless of the deposition thickness of molybdenum, the crystal structure of $CuInS_2$ and CdS was confirmed to be a chalcopyrite and zinc blend. Mo- or Ta-related phases are not detected, which is due to the formation of amorphous phases for $TaO_x$ or Mo by e-beam evaporation. Only an unassigned broad peak at ∼40.6° might be related to molybdenum or tantalum oxide, but it does not agree well with the XRD database because of the alloying of Mo and $TaO_x$. The cross-sectional TEM image clearly shows the amorphous $(Ta,Mo)_x(O,S)_y$ film, and the line profile shows that Mo is diffused into the $TaO_x$ layer.

To characterize a depth-specific element profile in detail, XPS analysis was carried out with $Ar^+$ bombardment. Figure 2 shows the binding energy of four atoms (Ta, Mo, O, S) vs a sputtering depth of 0−28 nm. Interestingly, the diffusion of Mo atoms into a tantalum oxide layer was found regardless of the Mo thickness deposited. However, tantalum atoms hardly diffused toward the surface. Oxygen atoms are continuously found on increasing the sputtering depth. Therefore, this indicates that molybdenum is present in a $MoO_x$ form near the


https://doi.org/10.1021/acsami.1c09560
ACS Appl. Mater. Interfaces XXXX, XXX, XXX−XXX

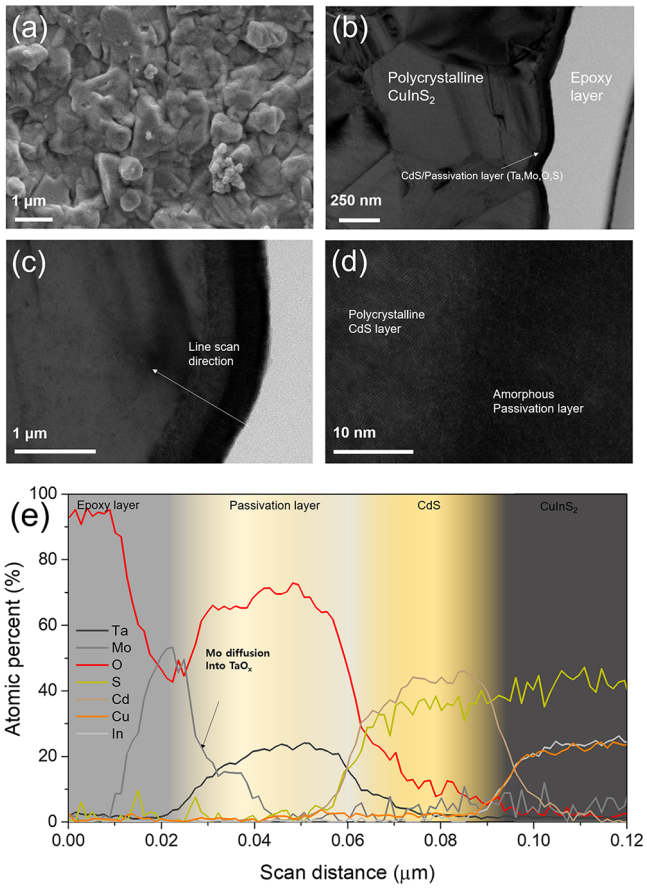


**Figure 1.** (a) SEM image of $CuInS_2/CdS/(Ta,Mo)_x(O,S)_y$ films with 6 nm molybdenum. The cross-sectional HR-TEM images of the same photoelectrode with low and high magnification for (b–d). EDS line profile results are shown in (e).

surface and a $(Ta,Mo)O_x$ form at deep layers of the film. Most of the sulfur atoms are found at the very surface of the film; this is due to the low sulfurization rate by $H_2S$ gas under a mild annealing condition (200 °C). On the other hand, only oxygen atoms from native molybdenum oxides are observed, and there is no observation of S atoms in the Mo film deposited without a $H_2S$ annealing process (Figure S3).

In the result of the atomic ratio by the sputtering depth, the atomic ratio of metals (Ta and Mo) and chalcogen atoms (O and S) indicates that near-surface (<~5 nm depth) is less metallic than a deeper layer for all of the photocathodes. This is due to Mo incorporation into the $TaO_x$ layer and surface sulfurization by annealing under the $H_2S$ atmosphere. The metal ratio (Ta/Mo) indicates that Mo atoms are present only at the surface, and Ta concentration is gradually increased with the sputtering depth. Therefore, it is concluded that the gradient alloy of Mo and $TaO_x$, which is Mo-rich at the surface, is formed after e-beam evaporation. Diffusion of Mo is not driven by the annealing process under the $H_2S$ atmosphere. The same gradient pattern of the atomic ratio for Ta and Mo is obtained from the film before/after annealing (Figure S3). It is considered that Mo vapor during the e-beam evaporation has energy high enough to react with $TaO_x$ layers. The atomic ratio of S and O indicates that S atoms are present in high concentrations at the surface. The increase of the atomic ratio for S atoms in deep layers is due to the CdS sublayer under the $TaO_x$ layer and not the diffusion of S atoms into the metal oxide matrix. Based on these depth profiles, it can be concluded that the layer of $(Ta,Mo)_x(O,S)_y$ on $CuInS_2/CdS$ has two distinguished structures: the Mo-gradient $TaO_x$ alloying layer, $(Ta,Mo)O_x$, and the molybdenum oxysulfide layer, $Mo(O,S)_x$.

**3.2. Photoelectrochemical Activity of the $CuInS_2$ Photocathode with a $(Ta,Mo)_x(O,S)_y$ Passive Layer.** The activity of each $CuInS_2$ photocathode with a $(Ta,Mo)_x(O,S)_y$ passive layer for photoelectrochemical hydrogen evolution was investigated under light illumination conditions (Figure 3). The activity of the photocathode is also compared to that of a controlled photocathode, $CuInS_2/CdS/TaO_x/Pt$, which is decorated with Pt and without Mo deposition. The photocurrent is strongly affected by the deposition thickness of molybdenum. In the cases of 2 and 30 nm Mo, only photocurrent of less than $-2$ mA $cm^{-2}$ is obtained even with cathodically increased applied potential. However, in the cases of 6 and 12 nm Mo, the photocurrent of more than $-10$ mA $cm^{-2}$ is obtained at 0 $V_{RHE}$ applied potential. The 6 nm Mo film shows the best photoelectrochemical activity; the photocurrent at 0 $V_{RHE}$ is $-11$ mA $cm^{-2}$, and the onset potential is 0.55 $V_{RHE}$. This photocurrent is about ~80% of that of the $CuInS_2/CdS/TaO_x/Pt$ photocathode (Figure 3b). Further, 0.67% of HC-ABPE for the $CuInS_2/CdS/(Ta,Mo)_x(O,S)_y$ photocathode (6 nm Mo) was also obtained from LSV results (Figure S4). Lower IPCE values were found from the $CuInS_2/CdS/(Ta,Mo)_x(O,S)_y$ (6 nm Mo) photocathode in the visible-light region when compared to $CuInS_2/CdS/TaO_x/Pt$; this might be due to the low transmittance property of $(Mo,Ta)_x(O,S)_y$ (Figure S5). This activity is one of the best photoelectrochemical performances among reported $CuInS_2$-based photocathodes for HER without a Pt cocatalyst or even with a Pt cocatalyst (refer to Table S2 and references in the Supporting Information).

*3.2.1. Charge Transfer Properties and Electrochemical Activity of the Passivation Layer.* Therefore, the detailed role of $(Ta,Mo)_x(O,S)_y$ for photoelectrochemical activity was investigated using (photo)electrochemical analysis. EIS analysis was conducted in a different potential range under the light illumination condition (Figure S6). The equivalent circuit, which is shown in Figure 4, is suggested to interpret the obtained EIS spectra. A series of two R-CPE circuits are used for the photocathodes, except for the 30 nm Mo deposited film, for which three R-CPE circuits are used. This is because an additional Mo-dominant oxide interlayer is generated at the Mo-gradient $TaO_x$ alloy layer with 30 nm Mo thickness (refer to Figure 2).

$R_{sol}$ is the solution resistance, $R_{semi}$ and $CPE_{semi}$ are the charge transfer resistance and the constant phase element at the internal semiconductor material, respectively, $R_{interface}$ and $CPE_{interface}$ are the charge transfer resistance and the constant phase element at the electrode/electrolyte interface, respectively, and $R_{interlayer}$ and $CPE_{interlayer}$ are the charge transfer resistance and the constant phase element at the $MoO_x$ interlayer in the $(Ta,Mo)_x(O,S)_y$ passive layer, respectively. As shown in Figure 4b,c, $R_{interface}$ is larger than $R_{semi}$ for all of the photocathodes, so the $R_{interface}$ rather than $R_{semi}$ is the bottleneck for the internal charge transfer at the semiconductor in the photoelectrochemical reaction. It is worth mentioning that the $R_{semi}$ increases with increasing Mo thickness when the $CuInS_2/CdS$ layer has an identical composition. This might be the light-shielding effect from the low transmittance of the $(Ta,Mo)_x(O,S)_y$ passive layer (Figure S5); the semiconductor


https://doi.org/10.1021/acsami.1c09560
ACS Appl. Mater. Interfaces XXXX, XXX, XXX–XXX

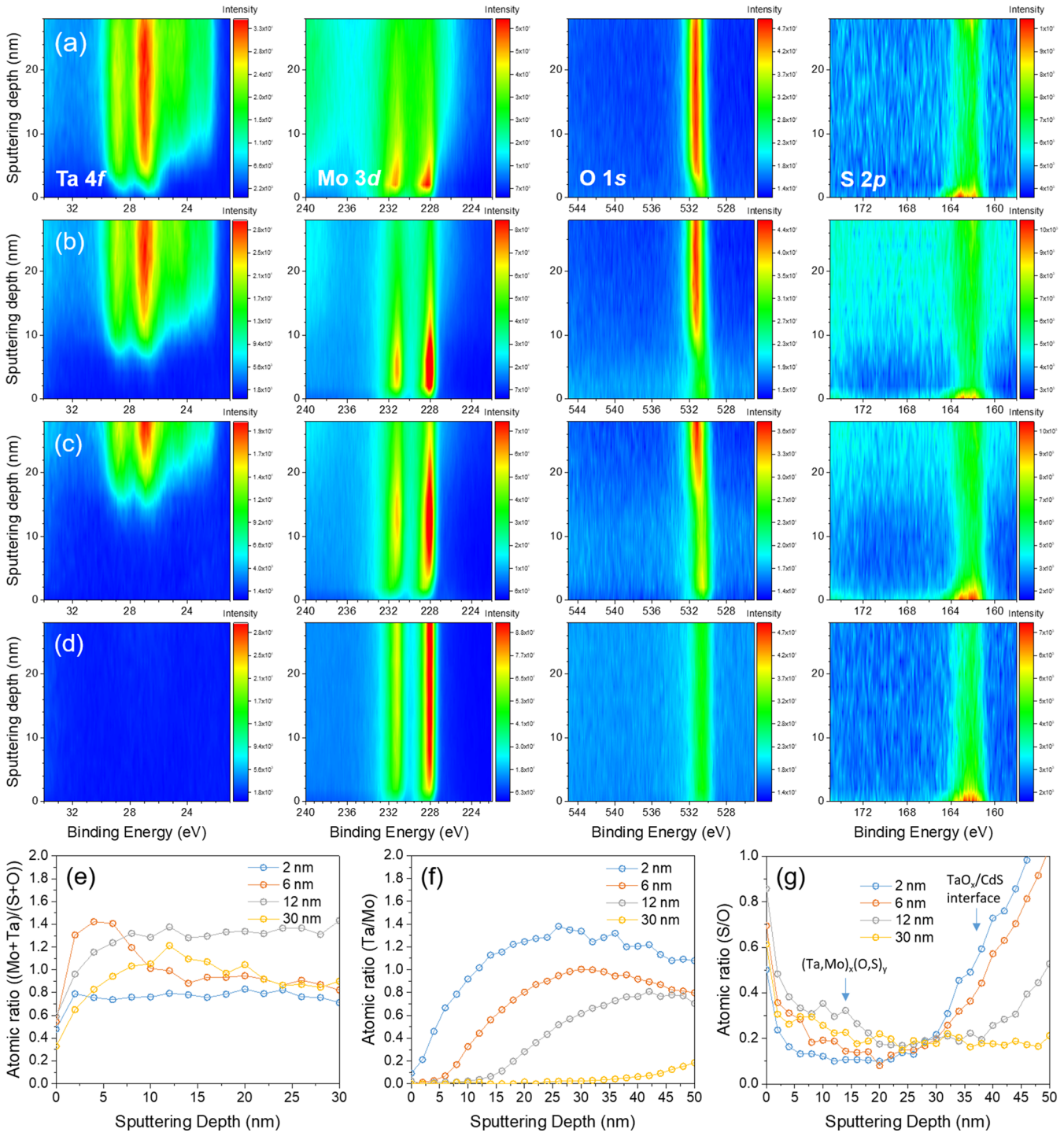


**Figure 2.** XPS spectra with the depth profiles of Ta 4f, Mo 3d, O 1s, and S 2p for the deposited Mo thicknesses of (a) 2 nm, (b) 6 nm, (c) 12 nm, and (d) 30 nm. The atomic ratio by XPS analysis depending on the sputtering depth and deposited Mo thickness (e–g).

has high conductivity due to the higher concentration of excited carriers at large photon flux.[25,26]

The trend of $R_{interface}$ values agrees with that of LSV results in Figure 3. The photocathode deposited with 6 nm Mo shows the lowest $R_{interface}$, while the photocathode with 2 nm Mo shows the highest $R_{interface}$. The charge transfer at the electrode/electrolyte interface is related to several factors: the surface kinetics of a (photo)electrochemical reaction, the surface state of the electrode, and the conductivity of passive layer materials.[21,27,28] These factors can be strongly related to the chemical composition of the surface layer of $(Ta,Mo)_x(O,S)_y$. According to the atomic ratio from XPS analysis, the surface atomic composition of $(Ta,Mo)_x(O,S)_y$ is $(Mo_{0.91}Ta_{0.09})_1(O_1S_{0.5})_{2.08}$, $Mo(O_1S_{0.69})_{1.82}$, $Mo_1(O_1S_{0.86})_{1.69}$, and $Mo_1(O_1S_{0.61})_{3.03}$ for 2, 6, 12, and 30 nm Mo thicknesses, respectively. Substitution of O atoms with S atoms induces the catalytic activity for HER on the $(Ta,Mo)_x(O,S)_y$ layer because an unannealed Mo-deposited $CuInS_2/CdS/(Ta,Mo)O_x$ photocathode shows an inferior photocurrent density (Figure S7).


https://doi.org/10.1021/acsami.1c09560
ACS Appl. Mater. Interfaces XXXX, XXX, XXX–XXX

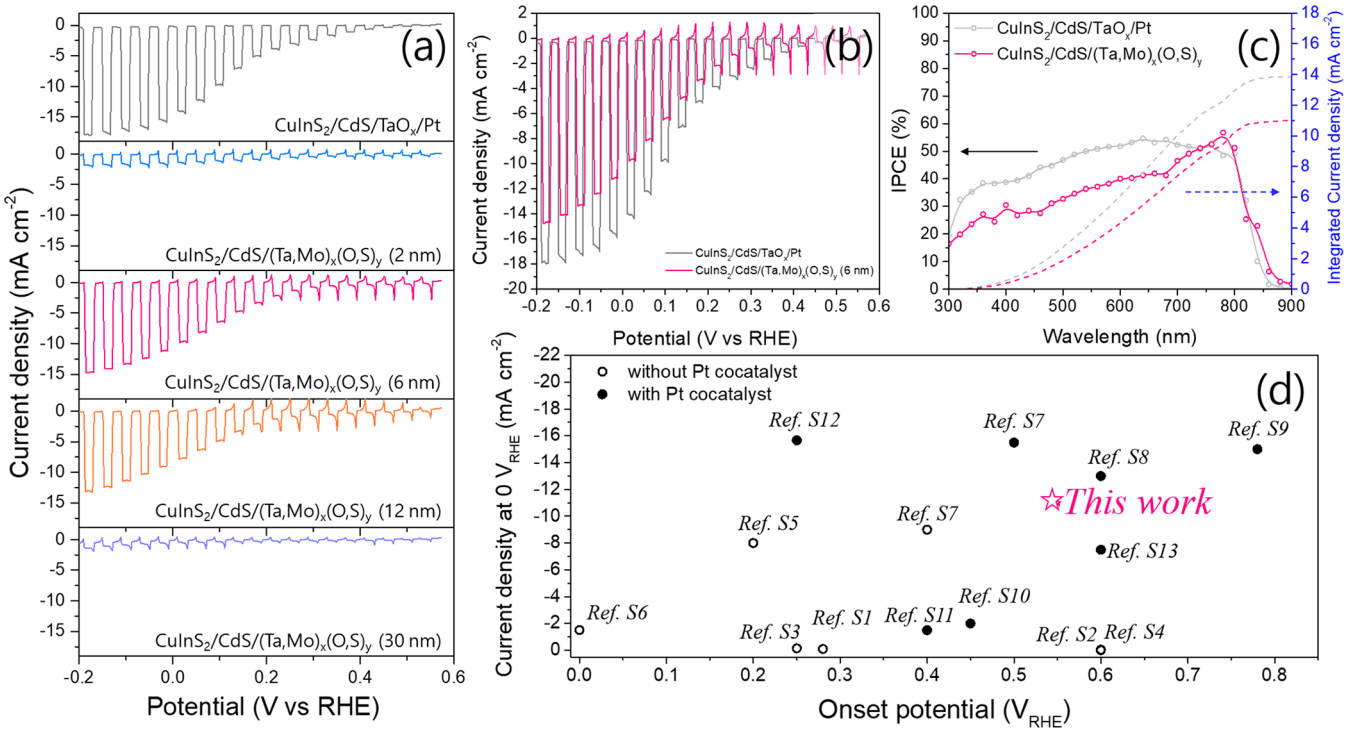


**Figure 3.** (a) LSV measurement for photocathodes under a light-chopping condition. (b) Photoelectrochemical activity of $CuInS_2$/CdS/$(Ta,Mo)_x(O,S)_y$ (6 nm) and $CuInS_2$/CdS/$TaO_x$/Pt photocathodes. (c) IPCE result with integrated current for $CuInS_2$/CdS/$(Ta,Mo)_x(O,S)_y$ (6 nm) and $CuInS_2$/CdS/$TaO_x$/Pt photocathodes. (d)Performance plot with reported $CuInS_2$-based photocathodes.

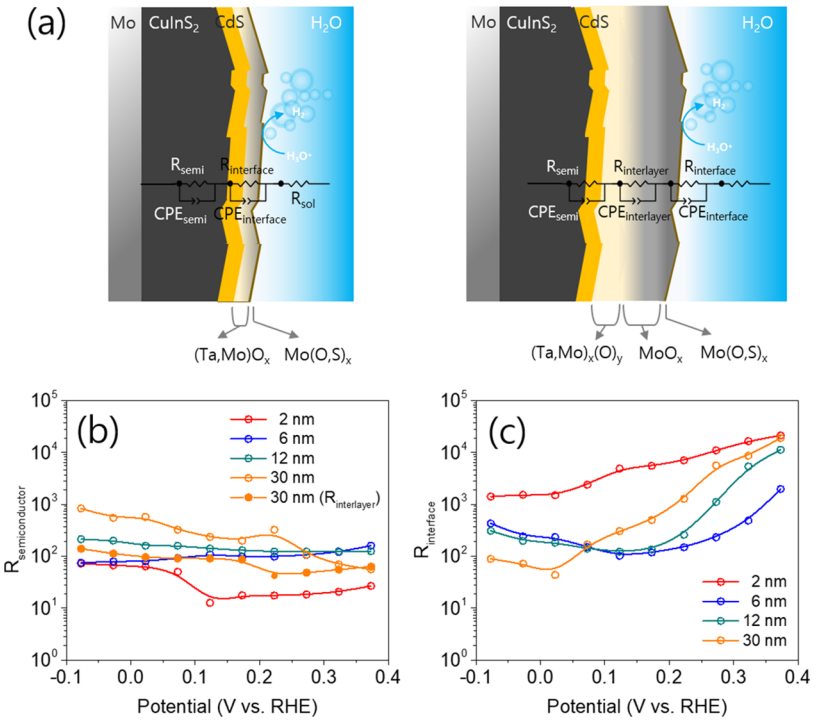


**Figure 4.** (a) Equivalent circuits and schematic diagrams for photocathodes (left panel, Mo deposition of 2−12 nm thickness; right panel, 30 nm thickness). (b) Charge transfer resistance at the internal semiconductor. The charge transfer resistance at the $MoO_x$ interlayer for a 30 nm Mo-deposited photocathode is also included. (c) Resistance at the electrode/electrolyte interface.

$MoS_{2-x}$ has been well known as the electrocatalytic material for HER.[23,29−31] Therefore, $MoS_x$ in the $(Ta,Mo)_x(O,S)_y$ matrix might contribute to the high electrocatalytic activity for HER. LSV measurement was carried out on an FTO/$(Ta,Mo)_x(O,S)_y$ electrode to investigate the electrocatalytic activity for HER only on the $(Ta,Mo)_x(O,S)_y$ layer (Figure S8). The best photoelectrochemical activity of the $(Ta,Mo)_x(O,S)_y$ photocathode is found at the 6 nm Mo film, and the best electrocatalytic activity ($\eta_{overpotential}$ = 415 mV at 5 mA·cm$^{-2}$ for HER) is observed at the 6 nm Mo-deposited


https://doi.org/10.1021/acsami.1c09560
ACS Appl. Mater. Interfaces XXXX, XXX, XXX−XXX

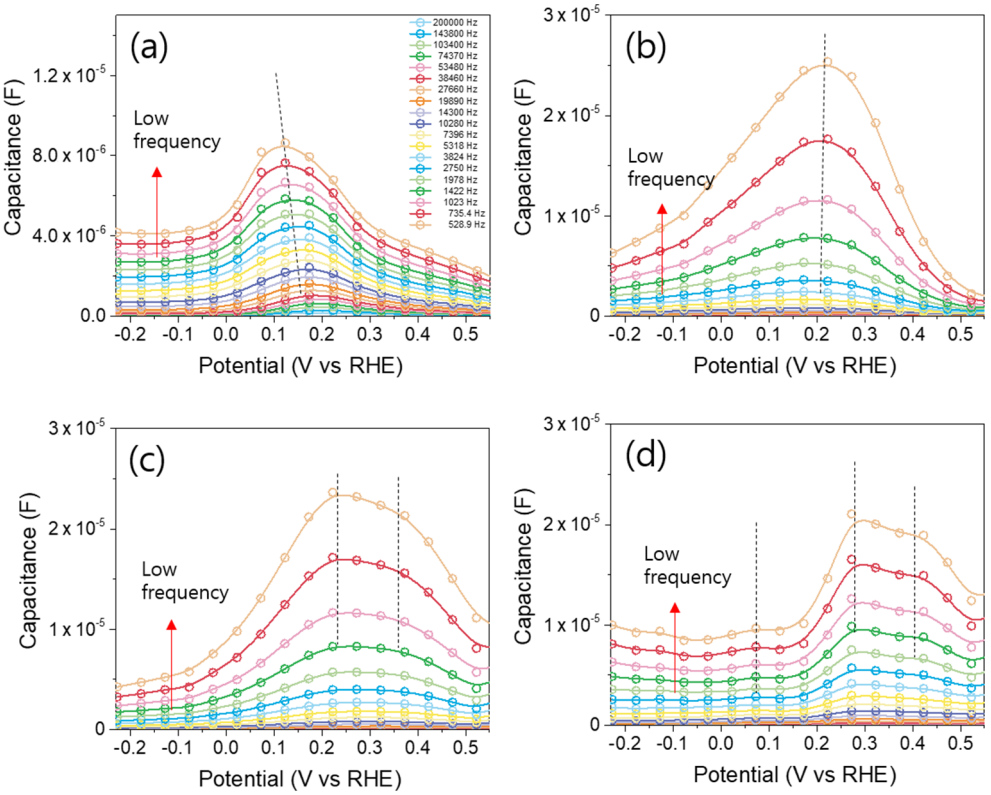


**Figure 5.** Capacitance−potential plot of a $CuInS_2/CdS/(Ta,Mo)_x(O,S)_y$ photocathode with deposited Mo thicknesses of (a) 2 nm, (b) 6 nm, (c) 12 nm, and (d) 30 nm. The dashed lines indicate the potential related to $C_{ss}$.

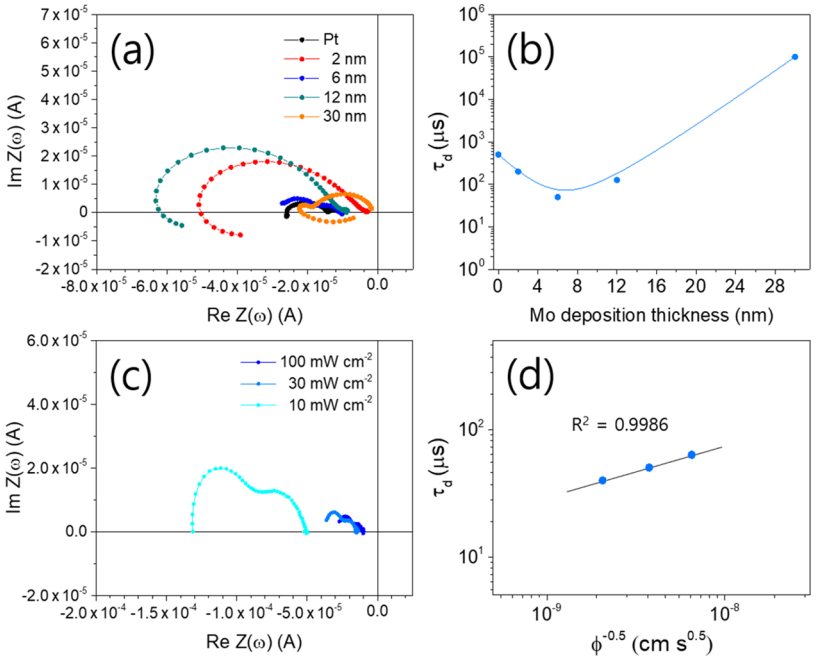


**Figure 6.** (a) Complex plots of IMPS results for $CuInS_2/CdS/TaO_x/Pt$ and $CuInS_2/CdS/(Ta,Mo)_x(O,S)_y$ photocathodes. (b) Plot of transient time ($\tau_d$) vs deposited Mo thickness for $CuInS_2/CdS/(Ta,Mo)_x(O,S)_y$ photocathodes. 0 nm indicates pure $TaO_x$, which is for a $CuInS_2/CdS/TaO_x/Pt$ photocathode. (c) Complex plot of IMPS for $CuInS_2/CdS/(Ta,Mo)_x(O,S)_y$ (6 nm) photocathodes with different light intensities. (d) log $\tau_d$ vs log $\Phi^{-0.5}$ plot for a $CuInS_2/CdS/(Ta,Mo)_x(O,S)_y$ (6 nm) photocathode. $\Phi$ is the photon flux of incident light during the IMPS measurement.

electrode of $(Ta,Mo)_x(O,S)_y$. The difference in electrochemical activity among the electrodes originates from the different chemical compositions; the HER activity of $MoS_2$ or $MoS_x$ can be significantly affected by S vacancies or oxygen doping levels in $MoS_x$.[32−34] In this stage, it is hard to conclude the relationship between the HER activity and the composition of $(Ta,Mo)_x(O,S)_y$, but at least the composition of $Mo(O_1S_{0.69})_{1.82}$ shows the highest activity for both electrocatalytic


https://doi.org/10.1021/acsami.1c09560
ACS Appl. Mater. Interfaces XXXX, XXX, XXX−XXX

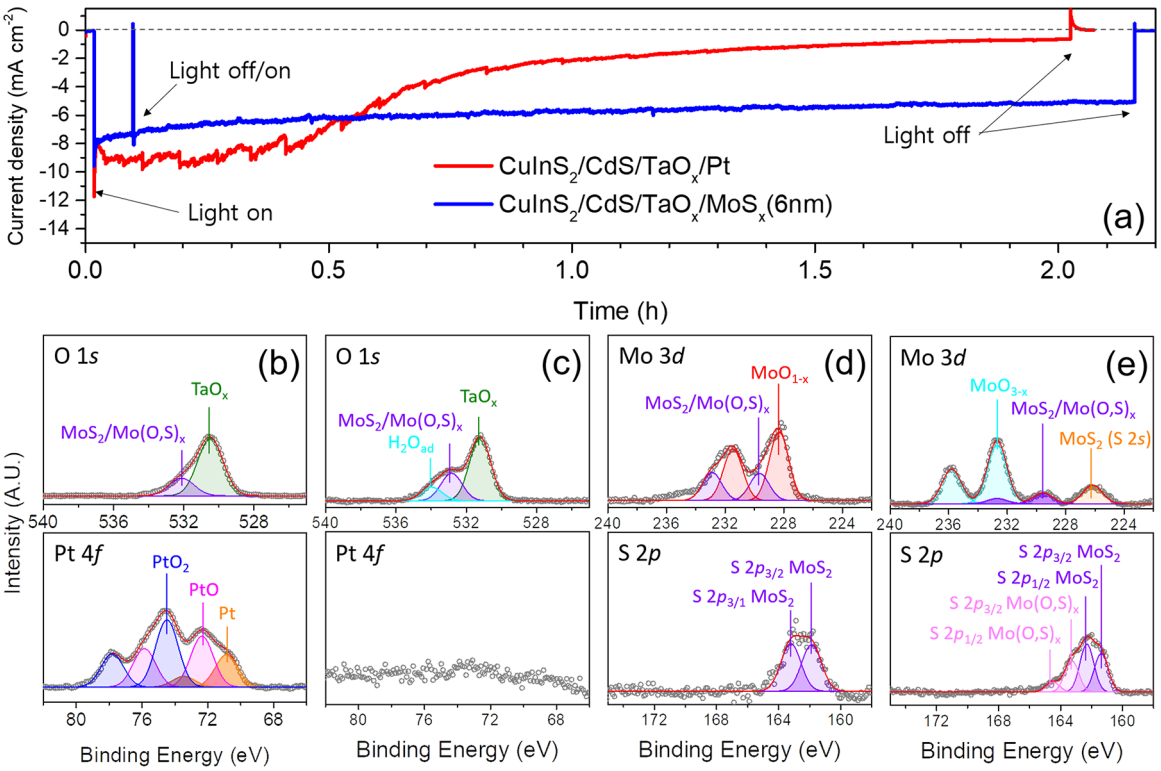


**Figure 7.** (a) Chronoamperometry result of $CuInS_2/CdS/TaO_x/Pt$ and $CuInS_2/CdS/(Ta,Mo)_x(O,S)_y$ photocathodes at 0 $V_{RHE}$ under the 1 sun illumination condition. XPS spectra of the (b) as prepared and (c) after chronoamperometry $CuInS_2/CdS/TaO_x/Pt$ photocathode surface. XPS spectra of the $CuInS_2/CdS/(Ta,Mo)_x(O,S)_y$ photocathode surface: (d) as prepared and (e) after chronoamperometry.

and photoelectrocatalytic reactions. Therefore, this unique composition, $Mo(O_1S_{0.69})_{1.82}$, might be one of the reasons that the 6 nm Mo-deposited photocathode shows the best activity.

*3.2.2. Kinetics and Mechanism of Electron Transportation in Passivation Layers.* However, even though the activity is inferior to the 6 nm Mo film, the other $FTO/(Ta,Mo)_x(O,S)_y$ electrodes (2, 12, and 30 nm cases) still show comparable electrocatalytic activity, unlike the photoelectrochemical activity. This means that other factors affect the photoelectrochemical activity of the $(Ta,Mo)_x(O,S)_y$ photocathodes with different compositions. Therefore, a capacitance–potential plot is obtained from the Mott–Schottky results with different frequencies (Figure 5). Ideally, the capacitance in the space charge region shows a Mott–Schottky relationship with the applied potential.[35] However, the presence of the surface state in the semiconductor leads to an unsatisfied Mott–Schottky relationship because the surface state induces extra frequency-dependent capacitance.[36]

Therefore, the energy level of surface states can be estimated from the capacitance–potential plot with different frequencies.[35,37] In the capacitance–potential plot, a frequency-dependent peak can be found at a specific potential. For the 2 nm Mo-deposited photocathode, the peak is found at ~0.2 $V_{RHE}$. This implies the energy level of surface states. For the 2 and 6 nm Mo-deposited photocathodes, only one energy level for surface states can be found at ~0.2 $V_{RHE}$, but the number of energy levels for surface states (capacitance peaks) is increased as two (at 0.2 and 0.35 $V_{RHE}$) and three (at 0.07, 0.32, and 0.42 $V_{RHE}$) for the 12 and 30 nm Mo-deposited films. This additional generation of surface-state energy levels may allow for a higher chance of Shockley–Read–Hall recombination due to the additional level of surface states. Of course, the higher number of energy levels for surface states does not directly imply a higher density of the surface state. Besides, every surface state does not spur charge carrier recombination; the shallow trap state can improve electron transportation while the deep trap state does not.[38−40] However, the capacitance of the 6, 12, or 30 nm Mo-deposited photocathodes shows a higher value (~$2 \times 10^{-5}$ F) than that of the 2 nm Mo-deposited film (~$9 \times 10^{-6}$ F) at the same frequency, for example, at 528.9 Hz. A higher capacitance generally implies a higher density of states. At least it can be said that the higher Mo concentration in $(Ta,Mo)_x(O,S)_y$ has a higher density of surface states; then, it influences the charge transfer resistance at the electrolyte interface ($R_{interface}$) due to higher charge recombination during the photoelectrochemical reaction.

For the detailed investigation of electron transport kinetics with surface-state energy levels, IMPS was carried out for the $CuInS_2/CdS/TaO_x/Pt$ or $CuInS_2/CdS/(Ta,Mo)_x(O,S)_y$ photocathode (Figure 6). From the IMPS results, the transient time ($\tau_d$), which is the time for electron transport, can be calculated for p-type photoelectrodes using eq 6, where $\tau_d$ is transient time, $\omega_{max}$ is the angular frequency when the magnitude of the imaginary photocurrent is maximum, and $f_{max}$ is the frequency when the magnitude of the imaginary photocurrent is maximum[41]

$$\tau_d = \frac{1}{\omega_{max}} = \frac{1}{2\pi f_{max}} \quad (6)$$

When compared to pure $TaO_x$, $\tau_d$ is significantly decreased in the gradient $(Ta,Mo)O_x$ films deposited with 2 and 6 nm Mo. This can be due to the incorporated Mo atoms improving the conductivity of $TaO_x$. However, $\tau_d$ is again increased by


https://doi.org/10.1021/acsami.1c09560
ACS Appl. Mater. Interfaces XXXX, XXX, XXX−XXX

Mo deposition thickness (12 and 30 nm). The best $\tau_d$ of a 6 nm Mo film might be related to the best conductivity stemming from the optimum atomic ratio of Mo−Ta−O in the 6 nm $(Ta,Mo)_x(O,S)_y$ passive layer because the conductivity of $MoO_x$ is strongly affected by its stoichiometry.[42,43] It is noted that the Pt cocatalyst and $Mo(O,S)_x$ at the very surface of each photocathode do not affect $\tau_d$ much because they mainly contribute to electron extraction at the electrolyte interface as cocatalysts and not to electron transportation in the bulk material.

Also, $\tau_d$ is related to the energy level for surface states, which is obtained from the capacitance−potential plot (Figure 5), if the charge transport mechanism in the $(Ta,Mo)_x(O,S)_y$ passive layer is trap-mediated diffusion. The energy level for surface states at ∼0.2 $V_{RHE}$, which is found at the 2 and 6 nm Mo photocathodes, might serve as a shallow trap and contribute to increase charge transportation in $TaO_x$. The increased density of states for the shallow trap (i.e., the increased capacitance) contributes to increased charge transportation at the 6 nm Mo film. However, the surface state with energy levels at 0.32−0.42 $V_{RHE}$ at the 12 and 30 nm Mo films may be a deep trap and a recombination center because $\tau_d$ is significantly increased by more than 10−1000 times when compared to $\tau_d$ at the 6 nm Mo film.

Therefore, the IMPS measurement under different light intensities was carried out to reveal the mechanism of charge transportation for the photocathode (Figure 6c,d). The linear dependency of $\log(\tau_d)$ and log(inverse square root of photon flux ($\Phi^{-0.5}$)) is predicted from the electron diffusion mechanism with trapping/detrapping of electrons at the localized state (surface state, defect, dopant, etc.).[44] The $\log(\tau_d)$ value obtained from $CuInS_2/CdS/(Ta,Mo)_x(O,S)_y$ has a linear dependency with $\log(\Phi^{-0.5})$, so the electron transportation in the $(Ta,Mo)_x(O,S)_y$ passive layer follows the trap-mediated diffusion mechanism.[44−46] According to the IMPS and capacitance−potential plot results, it is concluded that incorporation (2−6 nm) of a specific amount of Mo into $TaO_x$ increases the surface state, which becomes a shallow trap, and then electron transportation is improved. However, incorporation of Mo greater than 6 nm seems to have detrimental effects on electron transportation due to additional deep trap sites.

### 3.3. Photoelectrochemical Water Splitting and the Stability of $CuInS_2/CdS/(Ta,Mo)_x(O,S)_y$ Photocathodes.

A photoelectrochemical stability test was carried out for the $CuInS_2/CdS/(Ta,Mo)_x(O,S)_y$ photocathode (Figure 7a). The photocurrent of $CuInS_2/CdS/(Ta,Mo)_x(O,S)_y$ is observed to be 62% of the initial current density, while the photocurrent of a reference $CuInS_2/CdS/TaO_x/Pt$ photocathode rapidly decreases after ∼0.5 h. The peaks of deconvoluted XPS spectra, which are obtained from the photoelectrode before/after the stability test, are assigned to $TaO_x$, adsorbed $H_2O$, Pt, and $PtO_x$ for a $CuInS_2/CdS/TaO_x/Pt$ photocathode and then are assigned to MoO, $MoO_3$, $MoS_2$ or $Mo(O,S)_x$, and adsorbed $H_2O$ for a $CuInS_2/CdS/(Ta,Mo)_x(O,S)_y$ photocathode (Figures 7b−e and S9).

For the $CuInS_2/CdS/TaO_x/Pt$ photocathode, the main reason for deactivation is the delamination of Pt cocatalysts due to disintegration of $Pt/TaO_x$ interfaces or $TaO_x$ surfaces. The increased binding energy of Ta 4f and O 1s indicates the stoichiometry change of $TaO_x$ by a photoelectrochemically partial oxidation reaction. The increased hydroxyl and adsorbed water (O 1s, M−OH, and $H_2O$) also imply that the chemical bonding of $TaO_x$ varied during the photoelectrochemical reaction.[21] Notably, the Pt 4f spectrum is diminished after the stability test. SEM results show the delamination/disintegration of the $Pt/TaO_x$ or $TaO_x$ layer (Figure S10). This means that the platinum metal and its oxide forms fell off from the $TaO_x$ surface.[5,15]

In the case of $CuInS_2/CdS/(Ta,Mo)_x(O,S)_y$, the passivation layer still has cocatalytic activity until 2.5 h, which coincides with the reported result of the chemical resistance of $MoO_x$ even during the photoelectrochemical reaction. The noticeable change of binding energy is found in the Mo 3d spectra from $MoO_{1-x}$ to $MoO_{3-x}$. The suppression of $MoO_{1-x}$ after the reductive photoelectrochemical reaction is also observed from another study.[19] However, this increased oxidation state of molybdenum is unexpected under reductive reaction conditions and might rather be the result of a stoichiometry change from $Mo(O,S)_x$ to $MoO_x$. This chemical-state change of Mo atoms might be related to the morphology, which is increased roughness after the stability test (Figure S10). Sometimes, redeposition of the Pt metal dissolved from a Pt anode on the photocathode must be considered for examining activity and stability tests. However, no redeposition of Pt was confirmed by XPS data for the $CuInS_2/CdS/(Ta,Mo)_x(O,S)_y$ photocathode under our experimental conditions (Figure S11). Moreover, even though the surface of our photocathodes seems rough, we confirmed that a uniform and fully covered passive layer was deposited on $CuInS_2/CdS$ films by e-beam evaporation (refer to Figure S12, the cross-sectional TEM image of photocathodes with low magnification). Therefore, photocorrosion of $CuInS_2/CdS$ due to contact with electrolytes through pinhole sites is less likely the reason for deactivation for both photoelectrodes ($TaO_x$/Pt and $(Ta,Mo)_x(O,S)_y$) at least in this elapsed-time level.

Lastly, the faradic efficiency ($\eta_F$) of a photoelectrochemical cell was measured (Figure S13). The average $\eta_F$ is ∼93.6% for $H_2$ evolution on the $CuInS_2/CdS/(Ta,Mo)_x(O,S)_y$ photocathode and ∼97.4% for $O_2$ evolution on a counter electrode. The main reason for $\eta_F$ being below 100% might be some side reactions (photodegradation). The reaction is light-dependent because $H_2$ and $O_2$ gases are not produced anymore since the illuminated light is turned off.

## 4. CONCLUSIONS

In summary, the novel material $(Ta,Mo)_x(O,S)_y$ was prepared and applied to a $CuInS_2$ photocathode as a cocatalytic passivation layer for photoelectrochemical $H_2$ production. The e-beam evaporation of Mo on amorphous $TaO_x$ leads to spontaneous alloying of Mo and $TaO_x$ and the atomic gradient of Ta/Mo. The Mo atoms generate the additional surface state of shallow traps and enhance electron transportation. The formation of the thin layer of $Mo(O,S)_x$ at the $(Ta,Mo)O_x$ surface by $H_2S$ annealing shows the cocatalytic activity as an electrocatalyst for the HER. Moreover, the Mo atom incorporation into the $TaO_x$ layer also increases the photoelectrochemical stability compared to a $TaO_x$ layer. As a result, $(Ta,Mo)_x(O,S)_y$ effectively enhances electron transportation and extraction at the $CuInS_2/CdS$ layer. $CuInS_2/CdS/(Ta,Mo)_x(O,S)_y$ shows one of the best photoelectrochemical activities among reported $CuInS_2$-based photocathodes without Pt cocatalysts. We hope that the strategy of Mo incorporation into $TaO_x$ or even other metal oxide passive layers will be applied to various photoelectrodes or photo-


https://doi.org/10.1021/acsami.1c09560
ACS Appl. Mater. Interfaces XXXX, XXX, XXX−XXX

devices for improving carrier transportation and electrocatalytic reaction without precious metals.

## ■ ASSOCIATED CONTENT

### Supporting Information

The Supporting Information is available free of charge at https://pubs.acs.org/doi/10.1021/acsami.1c09560.

SEM image; XPS depth profile, Bode plot of EIS results, and LSV of photoelectrodes; HC-ABPE results; LSV of passivation layers and capacitance−potential plot; transmission spectra of passivation layers; faradic efficiency measurement results; and activity comparison table for reported $CuInS_2$ photoelectrodes (PDF)

## ■ AUTHOR INFORMATION


### Corresponding Author

**Oh-Shim Joo** − *Clean Energy Research Center, Korea Institute of Science and Technology, Seoul 02792, Republic of Korea;* orcid.org/0000-0001-7145-5246; Email: joocat@kist.re.kr

### Authors

**Sang Youn Chae** − *Institute of NT-IT Fusion Technology, Ajou University, Suwon 16499, Republic of Korea;* orcid.org/0000-0002-6936-2224

**Yoolim Kim** − *Clean Energy Research Center, Korea Institute of Science and Technology, Seoul 02792, Republic of Korea; Department of Chemical and Biological Engineering, Korea University, Seoul 02841, Republic of Korea*

**Eun Duck Park** − *Department of Chemical Engineering and Department of Energy Systems Research, Ajou University, Suwon 16499, Republic of Korea;* orcid.org/0000-0001-5959-1982

**Sang Hyuk Im** − *Department of Chemical and Biological Engineering, Korea University, Seoul 02841, Republic of Korea;* orcid.org/0000-0001-7081-5959

Complete contact information is available at: https://pubs.acs.org/10.1021/acsami.1c09560


### Author Contributions

#S.Y.C. and Y.K. contributed equally to this work.

### Notes

The authors declare no competing financial interest.

## ■ ACKNOWLEDGMENTS

This study was supported by the institutional program of the Korea Institute of Science and Technology (no. KIST-2E31241) and the C1 Gas Refinery Program through the National Research Foundation of Korea (NRF) funded by the Ministry of Science, ICT and Future Planning (no. 2015M3D3A1A01064899). This research was also supported by the Basic Science Research Program through the National Research Foundation of Korea (NRF) funded by the Ministry of Education (no. 2020R1I1A1A01073326).

## ■ REFERENCES


(1) Shay, J. L.; Tell, B.; Kasper, H. M.; Schiavone, L. M. *p-d* Hybridization of the Valence Bands of I-III-$VI_2$ Compounds. *Phys. Rev. B* **1972**, *5*, 5003−5005.

(2) Kalamaras, E.; Maroto-Valer, M. M.; Shao, M.; Xuan, J.; Wang, H. Solar carbon fuel via photoelectrochemistry. *Catal. Today* **2018**, *317*, 56−75.

(3) Xia, C.; Wu, W.; Yu, T.; Xie, X.; Van Oversteeg, C.; Gerritsen, H. C.; De Mello Donega, C. Size-Dependent Band-Gap and Molar Absorption Coefficients of Colloidal $CuInS_2$ Quantum Dots. *ACS Nano* **2018**, *12*, 8350−8361.

(4) Qin, L.; Li, D.; Zhang, Z.; Wang, K.; Ding, H.; Xie, R.; Yang, W. The determination of extinction coefficient of $CuInS_2$, and $ZnCuInS_3$ multinary nanocrystals. *Nanoscale* **2012**, *4*, 6360−6364.

(5) Liu, J.; Wei, Z.; Shangguan, W. Defects Engineering in Photocatalytic Water Splitting Materials. *ChemCatChem* **2019**, *11*, 6177−6189.

(6) Li, H.-M.; Wang, Z.-Y.; Jing, H.-J.; Yi, S.-S.; Zhang, S.-X.; Yue, X.-Z.; Zhang, Z.-T.; Lu, H.-X.; Chen, D.-L. Synergetic integration of passivation layer and oxygen vacancy on hematite nanoarrays for boosted photoelectrochemical water oxidation. *Appl. Catal., B* **2021**, *284*, No. 119760.

(7) Long, X.; Gao, L.; Li, F.; Hu, Y.; Wei, S.; Wang, C.; Wang, T.; Jin, J.; Ma, J. Bamboo shoots shaped FeVO4 passivated ZnO nanorods photoanode for improved charge separation/transfer process towards efficient solar water splitting. *Appl. Catal., B* **2019**, *257*, No. 117813.

(8) Seger, B.; Pedersen, T.; Laursen, A. B.; Vesborg, P. C. K.; Hansen, O.; Chorkendorff, I. Using $TiO_2$ as a Conductive Protective Layer for Photocathodic $H_2$ Evolution. *J. Am. Chem. Soc.* **2013**, *135*, 1057−1064.

(9) Paracchino, A.; Laporte, V.; Sivula, K.; Grätzel, M.; Thimsen, E. Highly active oxide photocathode for photoelectrochemical water reduction. *Nat. Mater.* **2011**, *10*, 456−461.

(10) Gao, L.; Cui, Y.; Vervuurt, R. H. J.; Van Dam, D.; Van Veldhoven, R. P. J.; Hofmann, J. P.; Bol, A. A.; Haverkort, J. E. M.; Notten, P. H. L.; Bakkers, E. P. A. M.; Hensen, E. J. M. High-Efficiency InP-Based Photocathode for Hydrogen Production by Interface Energetics Design and Photon Management. *Adv. Funct. Mater.* **2016**, *26*, 679−686.

(11) Zhang, K.; Ravishankar, S.; Ma, M.; Veerappan, G.; Bisquert, J.; Fabregat-Santiago, F.; Park, J. H. Overcoming Charge Collection Limitation at Solid/Liquid Interface by a Controllable Crystal Deficient Overlayer. *Adv. Energy Mater.* **2017**, *7*, No. 1600923.

(12) Tang, P.-Y.; Han, L.-J.; Hegner, F. S.; Paciok, P.; Biset-Peiró, M.; Du, H.-C.; Wei, X.-K.; Jin, L.; Xie, H.-B.; Shi, Q.; Andreu, T.; Lira-Cantú, M.; Heggen, M.; Dunin-Borkowski, R. E.; López, N.; Galán-Mascarós, J. R.; Morante, J. R.; Arbiol, J. Boosting Photoelectrochemical Water Oxidation of Hematite in Acidic Electrolytes by Surface State Modification. *Adv. Energy Mater.* **2019**, *9*, No. 1901836.

(13) Yoo, I.-H.; Lee, Y.-J.; Kalanur, S. S.; Seo, H. Assembly of nonstoichiometric molybdenum oxide on Si as p-n junction photocathode for enhanced hydrogen evolution. *Appl. Catal., B* **2020**, *264*, No. 118542.

(14) Jeon, D.; Kim, H.; Lee, C.; Han, Y.; Gu, M.; Kim, B.-S.; Ryu, J. Layer-by-Layer Assembly of Polyoxometalates for Photoelectrochemical (PEC) Water Splitting: Toward Modular PEC Devices. *ACS Appl. Mater. Interfaces* **2017**, *9*, 40151−40161.

(15) Chae, S. Y.; Lee, M.; Je Kim, M.; Cho, J. H.; Kim, B.; Joo, O.-S. p-$CuInS_2$/n-Polymer Semiconductor Heterojunction for Photoelectrochemical Hydrogen Evolution. *ChemSusChem* **2020**, *13*, 6651−6659.

(16) Young, J. L.; Steiner, M. A.; Döscher, H.; France, R. M.; Turner, J. A.; Deutsch, T. G. Direct solar-to-hydrogen conversion via inverted metamorphic multi-junction semiconductor architectures. *Nat. Energy* **2017**, *2*, No. 17028.

(17) Hikita, Y.; Nishio, K.; Seitz, L. C.; Chakthranont, P.; Tachikawa, T.; Jaramillo, T. F.; Hwang, H. Y. Band Edge Engineering of Oxide Photoanodes for Photoelectrochemical Water Splitting: Integration of Subsurface Dipoles with Atomic-Scale Control. *Adv. Energy Mater.* **2016**, *6*, No. 1502154.

(18) Feng, K.; Huang, D.; Li, L.; Wang, K.; Li, J.; Harada, T.; Ikeda, S.; Jiang, F. MoSx-CdS/Cu2ZnSnS4-based thin film photocathode for solar hydrogen evolution from water. *Appl. Catal., B* **2020**, *268*, No. 118438.

(19) Gu, J.; Aguiar, J. A.; Ferrere, S.; Steirer, K. X.; Yan, Y.; Xiao, C.; Young, J. L.; Al-Jassim, M.; Neale, N. R.; Turner, J. A. A graded catalytic−protective layer for an efficient and stable water-splitting photocathode. *Nat. Energy* **2017**, *2*, No. 16192.
(20) Zheng, J.; Lyu, Y.; Wang, R.; Xie, C.; Zhou, H.; Jiang, S. P.; Wang, S. Crystalline $TiO_2$ protective layer with graded oxygen defects for efficient and stable silicon-based photocathode. *Nat. Commun.* **2018**, *9*, No. 3572.
(21) Chae, S. Y.; Kim, S.; Joo, O.-S. Design of an amorphous $TaO_x$ multifunctional interfacial layer on photocathodes for photoelectrochemical $H_2$ evolution. *J. Mater. Chem. A* **2019**, *7*, 2041−2047.
(22) Deng, Y.; Ting, L. R. L.; Neo, P. H. L.; Zhang, Y.-J.; Peterson, A. A.; Yeo, B. S. Operando Raman Spectroscopy of Amorphous Molybdenum Sulfide ($MoS_x$) during the Electrochemical Hydrogen Evolution Reaction: Identification of Sulfur Atoms as Catalytically Active Sites for $H^+$ Reduction. *ACS Catal.* **2016**, *6*, 7790−7798.
(23) Li, G.; Zhang, D.; Qiao, Q.; Yu, Y.; Peterson, D.; Zafar, A.; Kumar, R.; Curtarolo, S.; Hunte, F.; Shannon, S.; Zhu, Y.; Yang, W.; Cao, L. All the Catalytic Active Sites of $MoS_2$ for Hydrogen Evolution. *J. Am. Chem. Soc.* **2016**, *138*, 16632−16638.
(24) Li, Y.; Wang, H.; Xie, L.; Liang, Y.; Hong, G.; Dai, H. $MoS_2$ Nanoparticles Grown on Graphene: An Advanced Catalyst for the Hydrogen Evolution Reaction. *J. Am. Chem. Soc.* **2011**, *133*, 7296−7299.
(25) Wadsworth, B. L.; Beiler, A. M.; Khusnutdinova, D.; Reyes Cruz, E. A.; Moore, G. F. Interplay between Light Flux, Quantum Efficiency, and Turnover Frequency in Molecular-Modified Photoelectrosynthetic Assemblies. *J. Am. Chem. Soc.* **2019**, *141*, 15932−15941.
(26) Haussener, S.; Hu, S.; Xiang, C.; Weber, A. Z.; Lewis, N. S. Simulations of the irradiation and temperature dependence of the efficiency of tandem photoelectrochemical water-splitting systems. *Energy Environ. Sci.* **2013**, *6*, 3605−3618.
(27) Díez-García, M. I.; Gómez, R. Investigating Water Splitting with $CaFe_2O_4$ Photocathodes by Electrochemical Impedance Spectroscopy. *ACS Appl. Mater. Interfaces* **2016**, *8*, 21387−21397.
(28) Carroll, G. M.; Gamelin, D. R. Kinetic analysis of photoelectrochemical water oxidation by mesostructured Co-Pi/$\alpha$-$Fe_2O_3$ photoanodes. *J. Mater. Chem. A* **2016**, *4*, 2986−2994.
(29) Grutza, M.-L.; Rajagopal, A.; Streb, C.; Kurz, P. Hydrogen evolution catalysis by molybdenum sulfides ($MoS_x$): Are thiomolybdate clusters like $[Mo_3S_{13}]^{2-}$ suitable active site models? *Sustainable Energy Fuels* **2018**, *2*, 1893−1904.
(30) Mabayoje, O.; Liu, Y.; Wang, M.; Shoola, A.; Ebrahim, A. M.; Frenkel, A. I.; Mullins, C. B. Electrodeposition of $MoS_x$ Hydrogen Evolution Catalysts from Sulfur-Rich Precursors. *ACS Appl. Mater. Interfaces* **2019**, *11*, 32879−32886.
(31) Li, G.; Zhang, D.; Yu, Y.; Huang, S.; Yang, W.; Cao, L. Activating $MoS_2$ for pH-Universal Hydrogen Evolution Catalysis. *J. Am. Chem. Soc.* **2017**, *139*, 16194−16200.
(32) Xie, J.; Zhang, J.; Li, S.; Grote, F.; Zhang, X.; Zhang, H.; Wang, R.; Lei, Y.; Pan, B.; Xie, Y. Controllable Disorder Engineering in Oxygen-Incorporated $MoS_2$ Ultrathin Nanosheets for Efficient Hydrogen Evolution. *J. Am. Chem. Soc.* **2013**, *135*, 17881−17888.
(33) Tsai, C.; Li, H.; Park, S.; Park, J.; Han, H. S.; Nørskov, J. K.; Zheng, X.; Abild-Pedersen, F. Electrochemical generation of sulfur vacancies in the basal plane of $MoS_2$ for hydrogen evolution. *Nat. Commun.* **2017**, *8*, No. 15113.
(34) Wang, X.; Zhang, Y.; Si, H.; Zhang, Q.; Wu, J.; Gao, L.; Wei, X.; Sun, Y.; Liao, Q.; Zhang, Z.; Ammarah, K.; Gu, L.; Kang, Z.; Zhang, Y. Single-Atom Vacancy Defect to Trigger High-Efficiency Hydrogen Evolution of $MoS_2$. *J. Am. Chem. Soc.* **2020**, *142*, 4298−4308.
(35) Chae, S. Y.; Park, S. J.; Han, S. G.; Jung, H.; Kim, C.-W.; Jeong, C.; Joo, O.-S.; Min, B. K.; Hwang, Y. J. Enhanced Photocurrents with ZnS Passivated Cu(In,Ga)$(Se,S)_2$ Photocathodes Synthesized Using a Nonvacuum Process for Solar Water Splitting. *J. Am. Chem. Soc.* **2016**, *138*, 15673−15681.
(36) Madou, M. J.; Loo, B. H.; Frese, K. W.; Morrison, S. R. Bulk and surface characterization of the silicon electrode. *Surf. Sci.* **1981**, *108*, 135−152.
(37) Winnerl, A.; Garrido, J. A.; Stutzmann, M. Electrochemical characterization of GaN surface states. *J. Appl. Phys.* **2017**, *122*, No. 045302.
(38) Xue, J.; Fujitsuka, M.; Majima, T. Shallow Trap State-Induced Efficient Electron Transfer at the Interface of Heterojunction Photocatalysts: The Crucial Role of Vacancy Defects. *ACS Appl. Mater. Interfaces* **2019**, *11*, 40860−40867.
(39) Jiang, C.; Moniz, S. J. A.; Wang, A.; Zhang, T.; Tang, J. Photoelectrochemical devices for solar water splitting—Materials and challenges. *Chem. Soc. Rev.* **2017**, *46*, 4645−4660.
(40) He, T.; Wang, L.; Fabregat-Santiago, F.; Liu, G.; Li, Y.; Wang, C.; Guan, R. Electron trapping induced electrostatic adsorption of cations: A general factor leading to photoactivity decay of nanostructured $TiO_2$. *J. Mater. Chem. A* **2017**, *5*, 6455−6464.
(41) Ponomarev, E. A.; Peter, L. M. A comparison of intensity modulated photocurrent spectroscopy and photoelectrochemical impedance spectroscopy in a study of photoelectrochemical hydrogen evolution at p-InP. *J. Electroanal. Chem.* **1995**, *397*, 45−52.
(42) Cauduro, A. L. F.; Fabrim, Z. E.; Ahmadpour, M.; Fichtner, P. F. P.; Hassing, S.; Rubahn, H.-G.; Madsen, M. Tuning the optoelectronic properties of amorphous $MoO_x$ films by reactive sputtering. *Appl. Phys. Lett.* **2015**, *106*, No. 202101.
(43) Sook Oh, M.; Seob Yang, B.; Ho Lee, J.; Ha Oh, S.; Soo Lee, U.; Jang Kim, Y.; Joon Kim, H.; Soo Huh, M. Improvement of electrical and optical properties of molybdenum oxide thin films by ultralow pressure sputtering method. *J. Vac. Sci. Technol., A* **2012**, *30*, No. 031501.
(44) De Jongh, P. E.; Vanmaekelbergh, D. Trap-Limited Electronic Transport in Assemblies of Nanometer-Size $TiO_2$ Particles. *Phys. Rev. Lett.* **1996**, *77*, 3427−3430.
(45) Schneider, C.; Liu, N.; Schmuki, P. Optimized FTO seeding enables the growth of highlyefficient Ta-doped $TiO_2$ nanorod photoanodes. *Chem. Commun.* **2017**, *53*, 10050−10053.
(46) Lynch, R. P.; Ghicov, A.; Schmuki, P. A Photo-Electrochemical Investigation of Self-Organized $TiO_2$ Nanotubes. *J. Electrochem. Soc.* **20**




https://doi.org/10.1021/acsami.1c09560
ACS Appl. Mater. Interfaces XXXX, XXX, XXX−XXX